Tizian Bucher[1]
Advanced Manufacturing Laboratory,
Department of Mechanical Engineering,
Columbia University,
New York, NY 10027
e-mail: tb2430@columbia.edu

Connor Finn
Advanced Manufacturing Laboratory,
Department of Mechanical Engineering,
Columbia University,
New York, NY 10027
e-mail: cmf2196@columbia.edu

Ravi Verma
Materials & Manufacturing Tech,
Boeing Research & Technology,
Berkeley, MO 63134
e-mail: ravi.verma2@boeing.com

Wayne Li
Boeing Company,
Philadelphia, PA 19078
e-mail: wayne.w.li@boeing.com

Y. Lawrence Yao
Fellow ASME
Advanced Manufacturing Laboratory,
Department of Mechanical Engineering,
Columbia University,
New York, NY 10027
e-mail: yly1@columbia.edu

3D Laser Forming of Metal Foam Sandwich Panels

Metal foam sandwich panels have been the subject of many concept studies, due to their exceptional stiffness, light weight, and crash absorption capacity. Yet, the industrial production of the material has been hampered by the fact that it is challenging to bend the material into practical engineering shapes. Only recently, it has been shown that bending of metal foam sandwich panels is possible using lasers. It was also shown that the material can be bent into Euclidean (2D) geometries, and the governing laser-induced bending mechanisms were analyzed. This study was focused on laser forming of metal foam sandwich panels into non-Euclidean (3D) geometries. It was investigated whether the bending mechanisms and process parameters identified for 2D laser forming translate to 3D deformation. Additionally, the impact of the laser scan length was determined by comparing different scan patterns that achieve the same 3D geometries. It was shown that laser forming could induce 3D deformation necessary for both bowl and saddle shapes, the two fundamental non-Euclidean geometries. The amount of laser-induced bending and in-plane strains vary depending on process conditions and the governing bending mechanisms. Lastly, the laser scan length was shown to become more important for metal foam sandwich panels, where the panel thickness tends to be large. [DOI: 10.1115/1.4047242]

Keywords: laser forming, sandwich panel, metal foam, 3D deformation, non-Euclidean geometry, numerical simulation, advanced materials and processing, laser processes, modeling and simulation, nontraditional manufacturing processes

1 Introduction

Throughout the past few decades, research studies have revealed that metal foam sandwich panels have an excellent stiffness, shock absorption capacity, and strength-to-weight ratio [1,2]. Additionally, sandwich panels are more easily integrable in engineering structures than freestanding metal foam, and their metallic "facesheets" protect the foam core. Due to these favorable properties, numerous potential applications have been identified for the material [3,4]. Many of these applications have started becoming realizable thanks to the efforts of recent studies, showing that laser forming can successfully bend the material up to high angles without inducing failure [5,6]. These studies performed a detailed analysis of the process window, the laser-induced bending mechanisms, and the bending efficiencies and limits at different process conditions. The impact of the sandwich panel manufacturing method was also discussed. While a lot of ground has been covered, the work thus far has been limited to straight-line laser scans and shaping of Euclidean (2D) geometries. In industrial applications, however, non-Euclidean (3D) geometries are often necessary to meet design requirements. Karmann GmbH [1,7], for instance, is working on car body structures that are largely made of metal foam sandwich panels, due to their exceptional stiffness, reduced weight compared to steel panels, and vibration damping properties. There has also been talk about using metal foam sandwich panels as cone-shaped adaptors to support the payload in manned rockets [4], or as structural components in various intricately shapes airplane components, as discussed in Sec. 2.2.

Those concept studies considered two near-net-shape manufacturing methods for the industrial application of sandwich panels. The first method is based on powder metallurgy [4]; metal and foaming agent powders are compressed inside a mold that has the desired shape. The resulting precursor is placed between solid metal sheets, which have also been stamped to the desired geometry. The assembly is then heated near the metal melting point, causing the foaming agent to release a gas that turns the precursor into foam. During foaming, the lateral expansion of the sandwich panel is restricted, giving rise to high pressures at the facesheet/foam core interface that promotes the formation of metallic bonds. While being able to manufacture a wide range of shapes, this process is only economic for a large production volume because it requires several molds. Additionally, the part size must be small, due to the high cost of large dies and the requirement of fitting the assembly into an oven. Another drawback is that the foam core cell distribution and density oftentimes becomes irregular during expansion and compression.

The second near-net-shape manufacturing method is 3D printing. Metal foam sandwich panels may either be 3D printed directly in the required shape, or a cast of the negative foam shape can be printed, out of which the foam can be cast [8]. Both approaches have the drawback that they are slow, can only manufacture relatively small parts, and are only applicable for low production volumes.

To overcome the aforementioned limitations, metal foam sandwich panels need to be manufactured in flat panels and subsequently be bent to the desired shape. Unfortunately, similar to 2D deformation, traditional bending methods are inherently unsuccessful at shaping 3D geometries. Hydroforming, for instance, causes severe foam crushing after forming sandwich panels into dome shapes [9]. Other traditional bending methods, such as die stamping

[1]Corresponding author.

Manuscript received April 14, 2019; final manuscript received April 5, 2020; published online June 2, 2020. Assoc. Editor: Hongqiang Chen.

[10], have not been attempted for 3D geometries, since they were unable to form 2D geometries without significant defects. In this study, laser forming was investigated for 3D geometries, building upon the success of the method at shaping metal foam sandwich panels in 2D [5,6].

To date, 3D laser forming has only been investigated for sheet metal. Most of the effort has been spent generating two fundamental 3D shapes, which are the bowl and saddle shapes. The outcome of 3D laser forming experiments has been studied for a wide range of scan patterns, scan speeds, spot sizes, and powers [11–14]. Similarly, process synthesis has been studied in great detail, where the scan pattern and process conditions are determined using finite element method (FEM) based on a principal strain-based method [15,16]. However, it has never been attempted to bend metal foam sandwich panels into 3D geometries using lasers.

In this study, it was investigated whether laser forming of 2D Euclidean geometries can be extended to forming 3D non-Euclidean geometries. It was analyzed whether the fundamental knowledge that has been acquired for 2D laser forming regarding the bending mechanisms and the process window translates to 3D laser forming. Finally, it was investigated whether the numerical modeling techniques that were developed in previous studies [5,6] remain applicable when 3D laser forming is concerned.

2 Background

2.1 Laser Forming of Euclidean Geometries. Previous studies have shown that laser forming can successfully bend metal foam sandwich panels into Euclidean (2D) geometries using a series of parallel and straight scans [5,6]. Euclidean geometries, such as the channel geometry shown in Fig. 1, only require bending strains, which arise if the strain distribution through the sheet thickness is non-uniform. As shown in Eq. (1), a bending strain vector $\underline{\varepsilon}_b$ develops if the minimum principal strain $\varepsilon_1^{s/2}$ at the top sandwich panel surface ($z = s/2$) differs from the minimum principal strain ε_1^0 at the mid-plane of the sandwich panel ($z = 0$)

$$\underline{\varepsilon}_b = \varepsilon_1^{s/2}\underline{n}_1^{s/2} - \varepsilon_1^0\underline{n}_1^0 \tag{1}$$

where s is the sandwich panel thickness, and $\underline{n}_1^{s/2}$ and $\underline{n}_1^0$ are the directional vectors at the top surface and the mid-plane of the sheet, respectively [16]. The minimum principal strain is used instead of the maximum principal strain because laser forming mostly induces compressive deformation perpendicular to the scan path [17].

Laser forming can generate Euclidean geometries with very large amounts of deformation and achieve bending angles up to 65 deg after repeated scans over single scan line. Additionally, small radii of curvature can be achieved, because the process shortens the top sheet segment relative to the bottom sheet segment, giving rise to large bending strains. The "shortening" is achieved through thermomechanical bending mechanisms that simultaneously occur in the top facesheet and the foam core. [5,6]. In the top facesheet, the bending mechanism depends on the process conditions. When the laser spot size is significantly smaller than the sandwich panel thickness, the laser-irradiated material in the facesheet undergoes extreme heating, while the surrounding material remains at room temperature. As a consequence, the thermal expansion of the heated material is suppressed and converted to plastic compressive strain. This mechanism is well known as the temperature gradient mechanism (TGM) [18]. If, on the other hand, the laser spot size is equal to or greater than the sandwich panel thickness, the top facesheet heats up more uniformly. The thermal expansion is again converted to plastic compressive strain, due to the heated material being restricted by the surrounding material, causing a thickening of the top facesheet relative to the bottom facesheet. This mechanism is commonly referred to as upsetting mechanism (UM).

In the foam core, the bending mechanism responsible for the compressive shortening is independent of the process condition [5,6,17]. The compressive shortening is driven by temperature gradients, analogous to the TGM. However, the thermal expansion is not converted to plastic compressive strain as in the TGM. Instead, the thermal expansion causes cell wall bending and collapse, as postulated by the modified temperature gradient mechanism (MTGM).

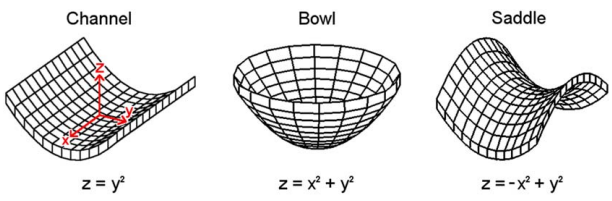

Fig. 1 The channel shape on the left is a Euclidean geometry. It can be obtained by bending strains alone, and the bending deformation is in the *yz*-plane. The bowl and saddle shapes are non-Euclidean geometries. Deforming a flat sheet into bowls and saddles requires both bending and in-plane strains, and the deformation occurs in three dimensions.

2.2 Shaping of Non-Euclidean Geometries. In many industrial applications, Euclidean (2D) geometries are not sufficient, and non-Euclidean (3D) geometries are required to realize design intents. Examples include airplane noses that could be used to protect aircraft against bird impacts [19] or airplane engine nacelles and car bodies [1]. Regardless of how complicated the 3D shape may be, it can be decomposed into the two fundamental non-Euclidean geometries, the bowl and saddle shapes (see Fig. 1). The airplane nose, for instance, has a distinct bowl shape, while the engine nacelle and car bodies consist of combinations of bowl and saddle shapes.

Unlike Euclidean geometries that have zero Gaussian curvature and only require bending strains, non-Euclidean geometries have a positive (e.g., bowl) or negative (e.g., saddle) Gaussian curvature. Hence, they require bending strains as well as in-plane strains, especially if a large amount of deformation is required [15,16]. Mathematically, Euclidean shapes only include deformation in one direction such as the channel ($z = y^2$), while non-Euclidean shapes require shortening (e.g., bowl, $z = x^2 + y^2$) or stretching (e.g., saddle, $z = -x^2 + y^2$) of the entire material section in the second coordinate direction, as shown in Fig. 1. Whether laser forming is capable of inducing those in-plane strains was the subject of this current investigation.

In order to specify scan patterns for the bowl and saddle shapes, inspiration was drawn from 3D laser forming of sheet metal. Several different approaches have been reported, depending on the complexity of the geometry. For simple geometries, such as the bowl shape, scan paths may be determined from laser forming principles. For all the bending mechanisms (TGM, UM, and MTGM) mentioned in Sec. 2.1, compressive shortening is induced near the top surface, and the material bends about the laser scan line towards the laser. This knowledge can be used to devise straightforward scan patterns, such as radial [11] or circular scan patterns [12]. A radial pattern, shown in Fig. 2(*a*), was used throughout Secs. 4.1–4.3 and contrasted with a circular scan pattern (Fig. 15) in Sec. 4.4. In both scan patterns, all the scans were performed on the top surface, represented by solid lines in Figs. 2(*a*) and 15. For the radial pattern, the scans were performed in an inward direction, terminating near the center of the specimen. The scans were initiated some distance away from the specimen edges to account for the delay between the laser shutter and the stage actuator. The scans were performed in the sequence indicated to allow for a smooth and more symmetric deformation of the entire specimen.

Using laser forming principles also allows for the determination of more complicated shapes such as the saddle shape, as was done in Ref. [13]. However, a more effective method of determining the

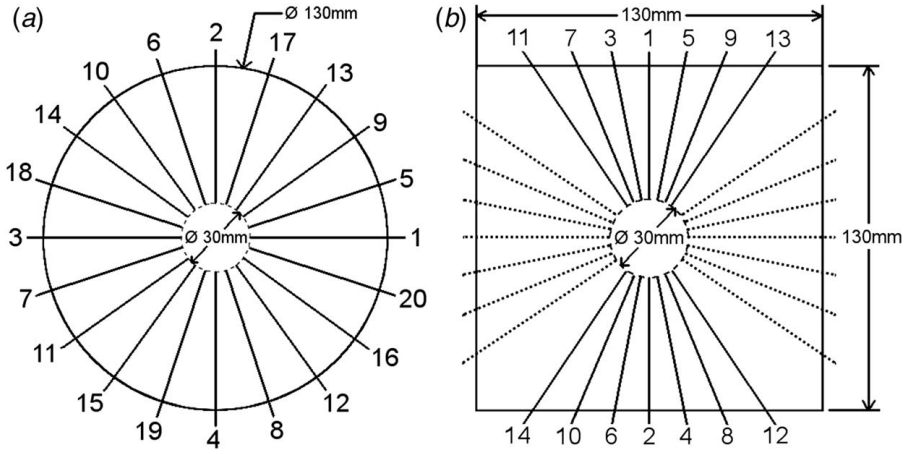

Fig. 2 Radial scan pattern that was used to obtain the (*a*) bowl shape and (*b*) saddle shape. Solid lines were performed on the top surface and dashed lines on the bottom surface. The numbering indicates the scan sequence. Scans were initiated on the outside and ended at the center. The diagrams apply for the condition of $D = 12$ mm and $v = 10$ mm/s. For $D = 4$ mm and $v = 30$ mm/s, the same overall area was treated, but the laser scans were closer together.

scan paths for complicated shapes is process synthesis, which was briefly mentioned in the Introduction [15,16]. In this approach, the desired geometry is modeled in FEM and compressed between rigid plates. Based on the resultant strain field, the scan paths can be drawn perpendicular to the directions of maximum plastic compressive strain. For a steel sheet of a thickness of 5 mm, this approach yielded a radial scan pattern [16] that was implemented in this study (see Fig. 2(*b*)) due to the high thickness of the sandwich panel of 10 mm. Since the deformation is bidirectional, half of the scans were performed on the top surface (solid lines in Fig. 2(*b*)), and half of the scans were performed on the bottom surface (dashed lines in Fig. 2(*b*)). The scans were performed in an inward direction, terminating near the center of the specimen.

For the process conditions, the same overall approach was pursued as in 2D laser forming [5]. Using the hypothesis that the bending mechanisms are not vastly different (to be discussed in Sec. 4.3), it was assumed that 3D laser forming could be performed with the same two process parameter regimes that were mentioned in Sec. 2.1. In the first regime, the laser spot size of $D = 4$ mm was small compared to the sandwich panel thickness, and an elevated scan speed of $v = 30$ mm/s was employed. In the second regime, the laser spot size of $D = 12$ mm was slightly greater than the sandwich panel thickness, and a slower scan speed of $v = 10$ mm/s was used to maintain a constant area energy of 6.66 J/mm^2. The laser power was maintained at $P = 800$ W for both conditions.

2.3 Numerical Simulation. The same constitutive relations and overall modeling approach was used as in 2D laser forming of Euclidean geometries [5]. The facesheets were assumed to be incompressible and were modeled using von Mises' yield criterion, von Mises' flow rule, and isotropic (strain) hardening. Facesheet material properties were extracted from Ref. [20].

The foam was modeled using an "equivalent" modeling approach, which used a straightforward cylindrical and rectangular geometry for the bowl (Fig. 3(*a*)) and saddle (Fig. 3(*b*)) shapes, respectively. The foam structure was not explicitly modeled to limit the computational intensity [6]. The foam behavior was modeled using the *crushable foam* constitutive model in ABAQUS. It was assumed that yielding can occur as a result of shear stresses, represented by von Mises' equivalent stress σ_e in the following yield criterion, and in hydrostatic compression, represented by the mean stress σ_m

$$F = \left[\frac{1}{1 + (\alpha/3)^2}(\sigma_e^2 + \alpha^2\sigma_m^2)\right]^{1/2} - Y \leq 0 \tag{2}$$

where α is the aspect ratio of the elliptical yield surface and Y is the flow stress [21]. The deformation is elastic if $F < 0$ and plastic if $F = 0$. It was further assumed that the plastic strain increment is perpendicular to the yield surface pursuant Drucker's postulate, yielding the following flow rule:

$$\dot{\varepsilon}_{ij}^p = \frac{\dot{Y}}{H}\frac{\partial F}{\partial \sigma_{ij}} \tag{3}$$

where $\dot{\varepsilon}_{ij}^p$ is the plastic strain rate and H is the hardening modulus that is described by

$$H = \frac{\sigma_e}{\hat{\sigma}}h_\sigma + \left(1 - \frac{\sigma_e}{\hat{\sigma}}\right)h_p \tag{4}$$

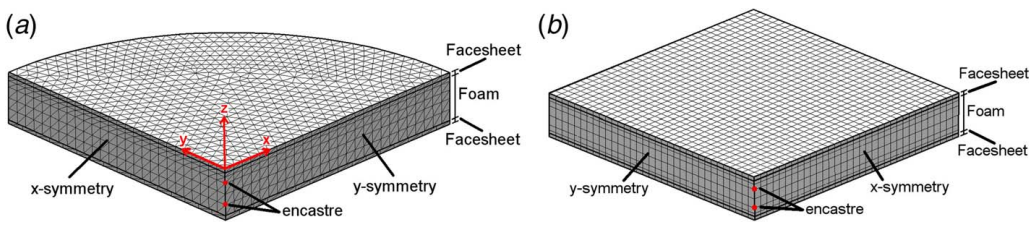

Fig. 3 (*a*) Bowl model and (*b*) saddle model. In both cases, only one-quarter of the specimen was modeled, and an *x* and *y* symmetry was employed. Both models were fixed at two vertically aligned points using encastre constraints.

where h_σ and h_p are the tangent moduli in uniaxial and hydrostatic compressions, respectively, and $\hat{\sigma}$ is equal to the first term in the yield criterion. A detailed discussion of all the assumptions and their validity may be found in Refs. [17,22], along with a list of sources for the metal foam material properties.

The interface between the facesheets and the foam core was modeled using a cohesive layer. Due to the infinitesimal thickness of this layer, tractions and separations were used at the interface instead of stresses and strains. A linear traction-separation law was used

$$\begin{bmatrix} t_n \\ t_s \\ t_t \end{bmatrix} = \begin{bmatrix} K_{nn} & 0 & 0 \\ 0 & K_{ss} & 0 \\ 0 & 0 & K_{tt} \end{bmatrix} \begin{bmatrix} u_n \\ u_s \\ u_t \end{bmatrix} \tag{5}$$

where t is the traction, u the separation (jump discontinuity), and K the penalty stiffness. The subscripts n, s, and t refer to the normal, first and second shear directions, respectively. A high stiffness of 850 GPa was assigned to the cohesive layer, so as to not affect the deformation behavior of the sandwich panel [23]. A temperature-dependent gap conductance relationship was used from Ref. [24], which is discussed in detail in Ref. [5].

Due to the large size of the specimens and the high number of laser scans, symmetry boundary conditions were assumed that allowed modeling a quarter of the bowl (Fig. 3(*a*)) and saddle (Fig. 3(*b*)) shapes. The symmetry boundary conditions assume no heat transfer across the symmetry plane, no translations perpendicular to the plane, as well as no out-of-plane rotations. Unlike in 2D laser forming, symmetry boundary conditions induce some amount of error in 3D laser forming, since the problem is inherently asymmetric. However, the errors are relatively small and the predictions are still consistent with experimental values, as will be shown later. In addition to the symmetry boundary conditions, the specimens were anchored at two vertically aligned points at the center, marked as "encastre" in Figs. 3(*a*) and 3(*b*).

As will be discussed in Sec. 3, the sandwich panel showed substantial variations in the foam core thickness and density. To account for those variations and make a comparison with experiments possible, the thickness of each bowl and saddle model was adjusted to match the experimental average for that particular process condition. Changes in Young's modulus, the flow stress, and the thermal conductivity with density were accounted for as well, using relations given in Ref. [17].

All the simulations were uncoupled into a thermal and mechanical part, which were performed subsequently, using the thermal results as initial condition for the mechanical analysis. Hence, it was assumed that heating due to the mechanical deformation is negligible. In the bowl model, DC3D10/C3D10 elements were used for the facesheets/foam core, and DC3D6/COH3D6 elements were used for the cohesive layer in the thermal and mechanical analyses, respectively. In the saddle model, DC3D20/C3D20R elements were used for the facesheets/foam core, and DC3D8/COH3D8 elements were used for the cohesive layer in the thermal and mechanical analyses, respectively. An absorption coefficient of $A = 0.6$ was used for the thermal analysis, and all the simulations were performed in the FEM software ABAQUS.

3 Experimental Methods

The aluminum foam sandwich panel that was used in this study was manufactured using a powder-metallurgy technique by Havel metal foam GmbH. In this method, aluminum and foaming agent (TiH_2) powders are compressed, and the resulting precursor is sandwiched between solid metal "facesheets." The assembly is then placed into an oven and heated near the metal-melting temperature. The elevated temperatures cause the foaming agent to release hydrogen gas, which creates bubbles and turns the precursor into foam. Simultaneously, the lateral expansion of the material is restricted, giving rise to substantial pressures that sinters the foam to the adjacent facesheets [4].

The facesheets were made of AW 5005, and their thickness was 1 mm. The foam core was made of AlSi10, and its thickness and density varied considerably, ranging between 8–10 mm and 500–650 kg/m^3, respectively. The total sandwich panel thickness was between 10 and 12 mm. To account for the variations in the foam thickness and density, two experiments were performed for each condition per geometry, making sure that the average thickness and density were comparable.

The bowl specimens were cut to a diameter of 130 mm, while the saddle specimens were cut to squares with side lengths of 130 mm. Both specimen types were mounted at the center using a tapped hole. All specimens were painted with black graphite paint to increase the laser absorption. The specimens were laser formed using a CO_2 laser with a wavelength of 10.6 μm. After each laser scan, the specimens were cooled to room temperature. The two process conditions that were contrasted were introduced in Sec. 2.2. Deflections were measured by attaching a dial indicator to a robotic stage. Cross sections were cut using a diamond saw and polished using 1200 grit sand paper before imaging.

4 Results and Discussion

4.1 Bowl Shape. Both process parameter regimes that were discussed in the background yielded a substantial amount of bending deformation, as shown in Figs. 4(*a*) and 4(*b*). For the regime employing the larger spot size of $D = 12$ mm, the scan pattern in Fig. 2(*a*) was used, which was repeated eight times to obtain 160 scans. For the regime employing the smaller spot size of $D = 4$ mm, a denser line pattern with 50 scan lines was used. This modification was made based on the assumption that the bending mechanisms in 2D and 3D laser forming are similar (to be discussed in Sec. 4.3) and that consequently less bending

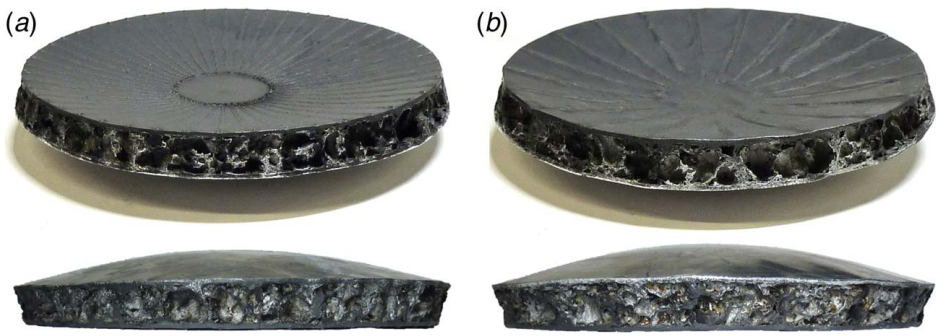

Fig. 4 Isometric and side view of the bowl shape (*a*) after 300 scans at a laser spot size of $D = 4$ mm with a scan speed of $v = 30$ mm/s and (*b*) after 160 scans at a laser spot size of $D = 12$ mm with a scan speed of $v = 10$ mm/s. The laser power was $P = 800$ W in both cases.

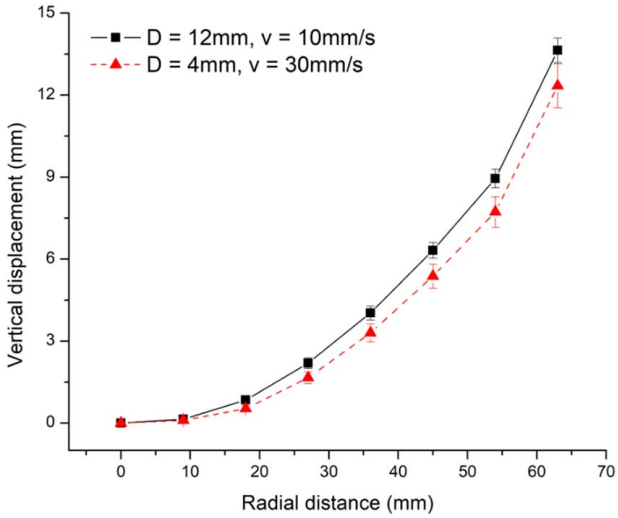

Fig. 5 Average radial deflection of the bowls in Fig. 4, shown with standard deviations. At a large spot size of $D = 12$ mm, a higher deflection was obtained even though the number of scans was lower than at a small spot size of $D = 4$ mm.

deformation is induced per scan line at $D = 4$ mm. The 50 scan line pattern was repeated six times to obtain a total of 300 scans.

Despite using nearly half the scans, more bending was achieved at $D = 12$ mm than at $D = 4$ mm, as shown in Fig. 5. Hence, for the same area energy, the deformation is more efficient at $D = 12$ mm. The same result was obtained for Euclidean geometries in Ref. [5], where several factors were identified to explain this difference in the bending efficiency. It was shown that the upsetting mechanism (UM), which governs the deformation of the top facesheet at $D = 12$ mm, induces plastic deformation over a larger region than the temperature gradient mechanism (TGM), which governs the deformation of the top facesheet at $D = 4$ mm. Similarly, it was shown that a larger segment of the foam core contributes to bending via the modified temperature gradient mechanism (MTGM) at $D = 12$ mm. Finally, it was shown that the bottom facesheet underwent more heat-induced softening at $D = 12$ mm, rendering the sandwich less resistant to bending deformation. In Sec. 4.3, it will be proven that all these factors are also valid for laser forming of non-Euclidean 3D geometries.

From Fig. 5, it can further be seen that the deviation in the bending deformation was slightly greater at $D = 4$ mm than at $D = 12$ mm. The same phenomenon was observed throughout the rest of the experimental results. Due to the localized plastic deformation occurring at $D = 4$ mm, the deformation of the top facesheet is more sensitive to the local foam structure, and hence, the deviations in the bending results are greater.

The process was numerically simulated, and a result is shown in Fig. 6. The simulation was carried out on a quarter of the circular specimen1 as shown in Fig. 3(*a*), and the visualization was based on mirroring the result in *x*- and *y*-directions. The deflection was magnified by a factor of 10 for viewing clarity, and only one iteration of the scan pattern in Fig. 2(*a*) was used. Despite using the symmetry constraints, laser scans lying on the symmetry planes yielded very similar plastic strain distributions as laser scans that were performed away from the symmetry planes.

Only one iteration of the radial scan pattern in Figs. 2(*a*) and 4(*a*) was performed at the spot sizes of $D = 12$ mm and $D = 4$ mm, respectively, shown in Fig. 7. The experimental data were averaged over two specimens. The thickness and density of the foam core were set equal to the experimental average, and the density-dependent material properties were adjusted accordingly. At $D = 12$ mm (Fig. 7(*b*)), a good agreement was achieved, while at $D = 4$ mm (Fig. 7(*a*)), the simulation overestimated the deformation, especially near the specimen edge. The same trends were observed for 2D laser forming of Euclidean geometries [5], where it was shown that the overestimation at $D = 4$ mm can be attributed to localized melting and paint removal that occurred due to elevated temperatures. Both of these factors reduced the experimental bending deformation but were neglected in the simulation.

4.2 Saddle Shape. Laser forming of saddle shapes was equally successful at both $D = 4$ mm and $D = 12$ mm, as shown in Figs. 8(*a*) and 8(*b*), respectively. At $D = 12$ mm, the pattern shown in Fig. 2(*b*) was used. This pattern of 28 scans was repeated six times, equating to a total of 168 scans, allowing a meaningful comparison with the bowl shape given in Fig. 4(*a*). At $D = 4$ mm, 48 scans were performed per iteration instead of 28 (12 per side instead of seven), due to the lower deformation per scan as discussed in Sec. 4.1. The laser-treated area was the same as at $D = 12$ mm, maintaining the same distance between the outermost scans and the edges, but the scans were performed closer to one another because the deformation is more localized for this process condition. The scan pattern was repeated six times to obtain a total of 288 scans, which is again comparable with the number of scans used in forming the bowl shape as in Fig. 4(*b*).

Figure 9 shows the deflection of the outer edges (defined as *edge* 1 and *edge* 2 in Fig. 10), which were averaged over both sides. Just like for the bowl shapes, $D = 12$ mm yielded significantly more bending than $D = 4$ mm, despite being bent with fewer scans and using the same area energy. The reason for this behavior is the same as discussed in Sec. 4.1.

Moreover, it is evident from Fig. 9 that the overall deflection in the saddle shape was smaller than that in the bowl shape (Fig. 5). At $D = 12$ mm, for instance, the maximum deflection in the saddle shape was 6.7 mm, less than half the maximum deflection of 13.6 mm for the bowl shape. This discrepancy is due to the deformation taking place in two opposite directions. Particularly near the specimen diagonals, the material is simultaneously pulled in the positive and negative *z*-directions. Hence, the deformation induced by the top surface scans to some extent negates the deformation induced by the bottom surface scans and vice versa. This effect

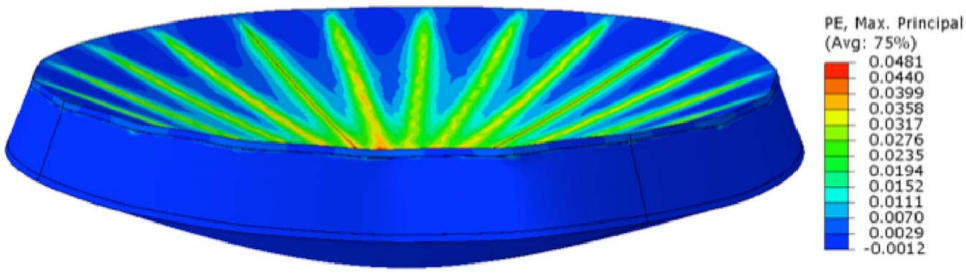

Fig. 6 Bowl shape predicted by the numerical model in Fig. 3(*a*), after performing one iteration of the scan pattern in Fig. 2(*a*). The model was mirrored in *x*- and *y*-directions. The spot size was $D = 12$ mm, and the scan speed was $v = 10$ mm/s. The deformation was magnified by a factor of 10 for viewing clarity.

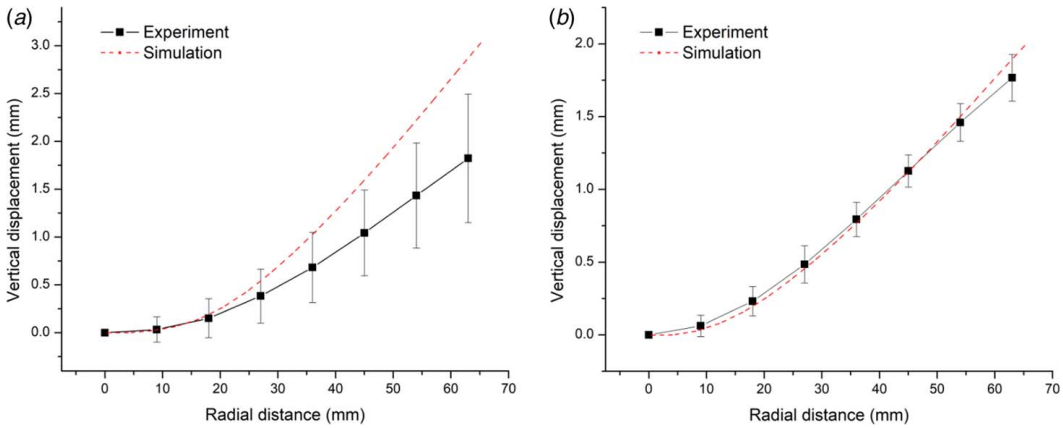

Fig. 7 Comparison of experimental and numerical deflections of the bowl shape at (*a*) a laser spot size of $D = 4$ mm with a scan speed of $v = 30$ mm/s and (*b*) a laser spot size of $D = 12$ mm with scan speed of $v = 10$ mm/s. One iteration of the scan pattern in Figs. 2(*a*) and 4(*a*) was performed. Average deflections and standard deviations are shown for the experimental data.

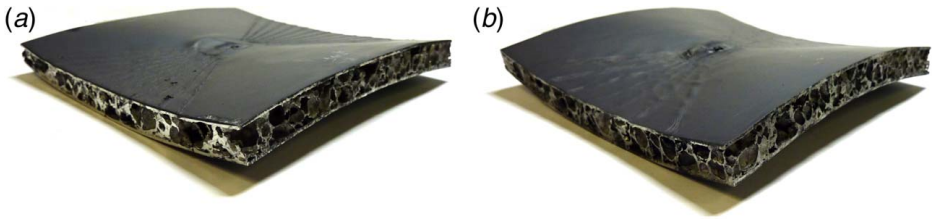

Fig. 8 Saddle shape (*a*) after 288 scans at a laser spot size of $D = 4$ mm with a scan speed of $v = 30$ mm/s and (*b*) after 168 scans at a laser spot size of $D = 12$ mm with a scan speed of $v = 10$ mm/s. The laser power was $P = 800$ W in both cases.

becomes less important as the specimen size and the distances between top surface and bottom surface laser scans are increased.

Numerical simulations were capable of predicting the saddle shape, as shown in Fig. 10, with the aid of symmetry conditions. Due to the computational intensity of the saddle model (Fig. 3(*b*)), which was larger and required more elements than the bowl model, only every other scan line was modeled that is shown in Fig. 2(*b*). The plastic strain distribution in Fig. 10 again looks uniform on all scan lines, regardless of whether the laser scans were performed on or away from the symmetry planes.

The comparison with experimental data, shown for $D = 4$ mm and $D = 12$ mm in Figs. 11(*a*) and 11(*b*), respectively, again showed a better agreement at the latter condition. The experimental results were averaged over two specimens for each condition, and the numerical models were adjusted for the foam core thickness and density. At $D = 4$ mm, the bending angles were again overestimated, due to the same reasons that were discussed in Sec. 4.1.

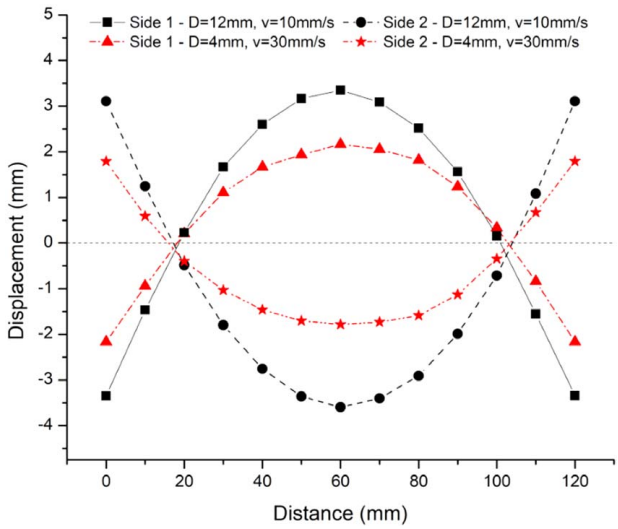

Fig. 9 Average deflection of the saddles in Fig. 8, measured at the outer edges marked as *edge* 1 and *edge* 2 in Fig. 10. The large spot size of $D = 12$ mm again yielded a higher amount of deformation than the small spot size of $D = 4$ mm.

4.3 Bending Mechanism. In order to analyze the bending mechanism, the thermal and mechanical response of the metal foam sandwich panel was investigated during laser forming. All the results in this section were obtained for the bowl shape but are valid for the saddle shape as well.

The thermal response was analyzed using the numerical results in Fig. 12, which shows the temperature distribution that establishes across the sandwich panel as the laser passes the cross section. At $D = 12$ mm, there is hardly any gradient across the top facesheet, implying that the thermal prerequisites for the UM are met. At $D = 4$ mm, on the other hand, a steep temperature gradient established across the top facesheet, meeting the prerequisites for the TGM. Across the foam core, there is a steep temperature gradient at both process conditions, satisfying the requirements of the MTGM. Hence, the thermal response of the sandwich panel suggests that the top facesheet and the foam core bend via separate bending mechanisms, which are the TGM/UM and the MTGM, respectively.

To confirm the findings from the thermal analysis, cross sections that were cut perpendicular to the laser scan direction were

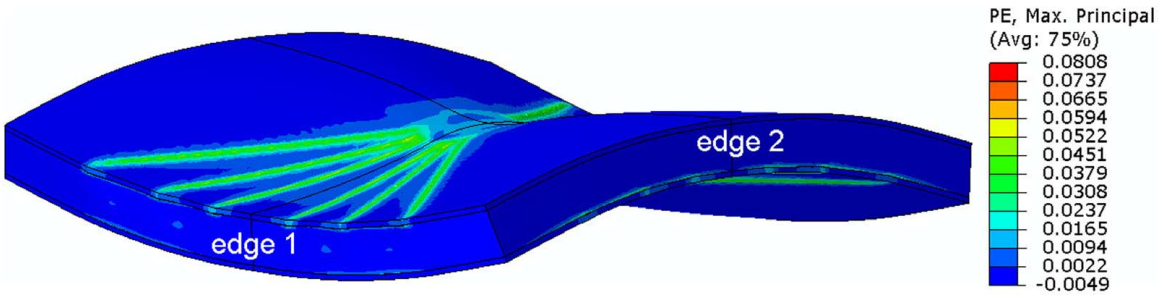

Fig. 10 Saddle shape predicted by the numerical model in Fig. 3(*b*) after mirroring the result in both *x*- and *y*-directions. The spot size was $D = 4$ mm and the scan speed was $v = 30$ mm/s. The deformation was magnified by a factor of 10 for viewing clarity. Only half the scans of Figs. 8 and 9 were modeled, skipping every other scan, to reduce the computational intensity.

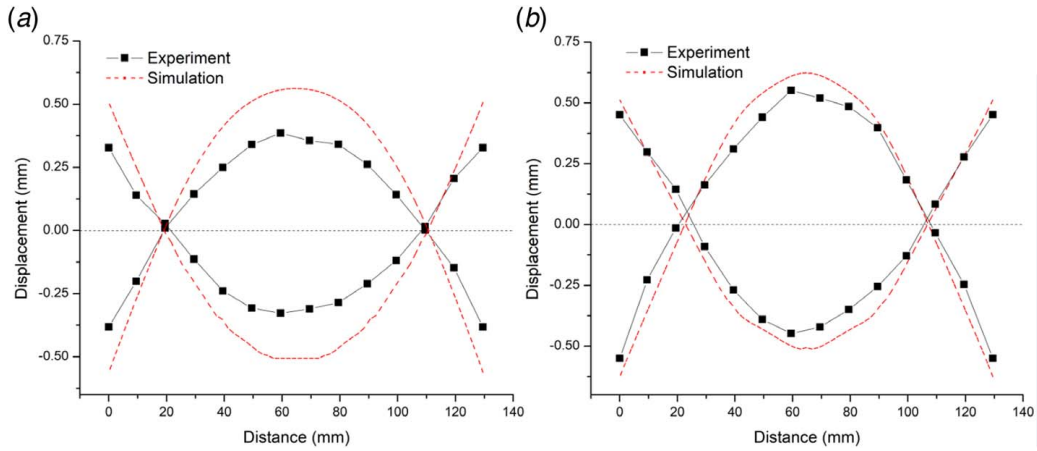

Fig. 11 Comparison of experimental and numerical deflections of the saddle shape at (*a*) a laser spot size of $D = 4$ mm with a scan speed of $v = 30$ mm/s and (*b*) a laser spot size of $D = 12$ mm with a scan speed of $v = 10$ mm/s after one iteration of the scan pattern. Average deflections are shown for the experimental data.

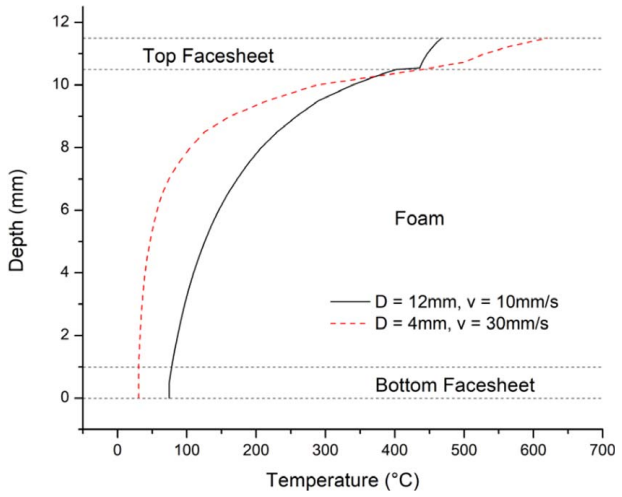

Fig. 12 Temperature distributions across the sandwich panel thickness right as the laser passes the cross section, predicted by the numerical models. At $D = 12$ mm, there is hardly any gradient across the top facesheet, satisfying the thermal prerequisites for the UM. At $D = 4$ mm, there is a steep gradient across the top facesheet, satisfying the thermal prerequisites for the TGM. In both cases, there is a steep gradient across the foam, satisfying the thermal prerequisites for the MTGM.

analyzed. At $D = 4$ mm (Fig. 13(*a*)), the top facesheet thickened slightly both into the foam core ($-z$-direction) and away from the foam core ($+z$-direction). The former is characteristic for the TGM, while the latter was also observed in 2D laser forming and was attributed to several factors [5]. First, the thermal expansion of the top facesheet during the laser scan is not suppressed, allowing the top facesheet to undergo some thickening in the negative z-direction. Second, the foam core densifies via the MTGM, leaving a void that needs to the filled by the top facesheet, leading to its thickening in the negative z-direction. Third, the foam core bends at a lower rate than the top facesheet and thus limits the amount of tensile stretching the top facesheet can undergo on the bottom surface. This leads to a shear traction that the foam core exerts onto the top facesheet, which can also promote an expansion of the top facesheet into the foam core. At the larger spot size of $D = 12$ mm, whose cross section is shown in Fig. 13(*b*), the top facesheet also thickened in both directions similar to $D = 4$ mm. At the same time, the thickening occurred over a larger material section, which was shown to be characteristic for the UM [5].

Numerical simulations confirmed the aforementioned findings. Figures 14(*a*) and 14(*b*) show the plastic strain distributions for $D = 4$ mm and $D = 12$ mm, respectively, at a cross section in the yz-plane midway through the laser scan. Only half of the specimen is shown because the laser scan was located on the symmetry plane. It can be seen that a larger segment of the top facesheet underwent plastic compression at $D = 12$ mm than did at $D = 4$ mm, where the

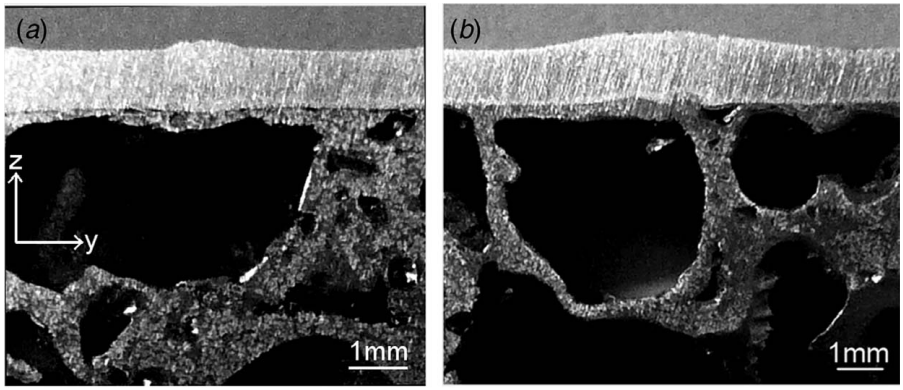

Fig. 13 Cross sections cut perpendicular to the scan path at (*a*) $D = 4$ mm and $v = 30$ mm/s and (*b*) $D = 12$ mm and $v = 10$ mm/s. The laser was scanned into the page. The cross sections look very similar to those obtained in 2D laser forming [5].

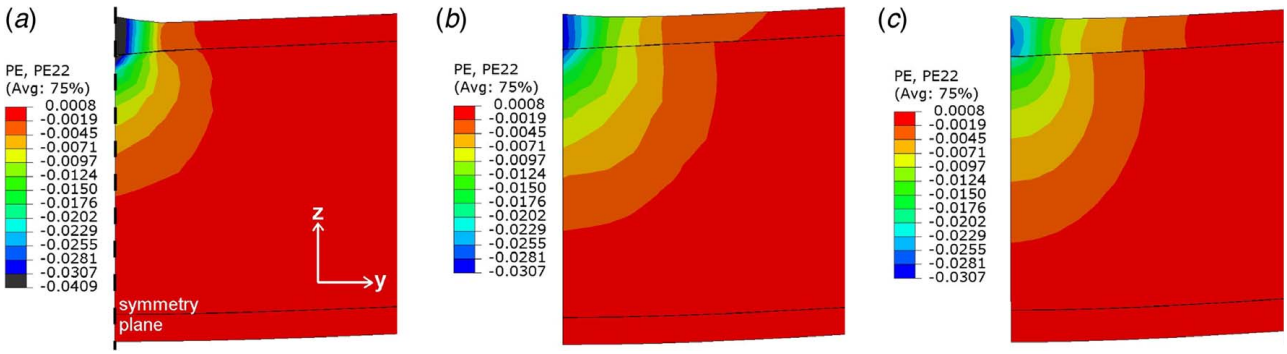

Fig. 14 Plastic strain distributions in *y*-direction (PE22) at a cross section that is perpendicular to the laser scan at (*a*) $D = 4$ mm and $v = 30$ mm/s (3D case), (*b*) $D = 12$ mm and $v = 10$ mm/s (3D case), and (*c*) $D = 12$ mm and $v = 10$ mm/s (2D case). The laser scan was performed on the symmetry plane; hence, only half of the specimen is shown. The deformation was magnified by a factor of 10 for viewing clarity. The foam thickness differed between the 2D (*c*) and 3D (*a*,*b*) cases to reflect the experimental specimens used.

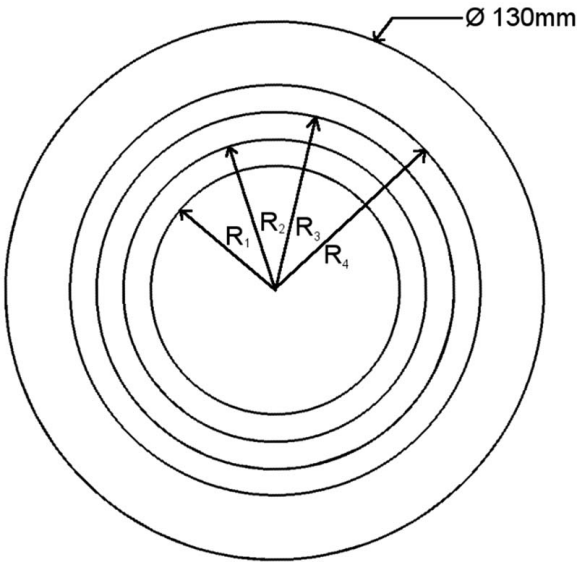

Fig. 15 Circular scan pattern that was used to obtain the bowl shape at $D = 12$ mm and $v = 10$ mm/s. The overall scan length is the same as in the radial scan pattern of Fig. 2(*a*). The radii are $R1 = 30$ mm, $R2 = 36.5$ mm, $R3 = 43.1$ mm, and $R4 = 49.6$ mm. At $D = 4$ mm and $v = 30$ mm/s, the same overall area was treated, but 10 laser radii were used that were closer to one another.

plastic compression was more localized near the scan line. This again confirms that the former case is governed by the UM while the latter is governed by the TGM. In the foam core, the plastic strain distribution was very similar to the distribution obtained in laser forming of freestanding metal foam [17], verifying that the MTGM was the governing mechanism. The bottom facesheet was again the only component that deformed due to the bending moment exerted by the top facesheet and the foam core, rather than a laser-induced bending mechanism.

Overall, the thermal and mechanical response of metal foam sandwich panels during 2D and 3D laser forming is nearly identical, both qualitatively and quantitatively. Qualitatively, the bending mechanisms are analogous, since the phenomena during 3D deformation shown in Figs. 12–14 are identical to those observed during 2D laser forming [5]. Quantitatively, nearly the same amount of plastic compressive strains are induced in 2D and 3D deformations, as shown in Figs. 14(*b*) and 14(*c*), respectively.

The bending and in-plane strains required for 3D deformation as stated in Sec. 2.2 depend on process conditions. Laser spot sizes of $D = 4$ mm and $D = 12$ mm were considered. At $D = 4$ mm, the deformation in the top facesheet (TGM) and the foam core (MTGM) only involved bending strains, and a moderate amount of deformation was achieved, as shown in Figs. 4(*b*) and 8(*b*). At $D = 12$ mm, the bending strains in the top facesheet were largely replaced by in-plane strains (UM). Hence, the compressive shortening in the top facesheet was more efficient, and a slightly larger amount of deformation was achieved.

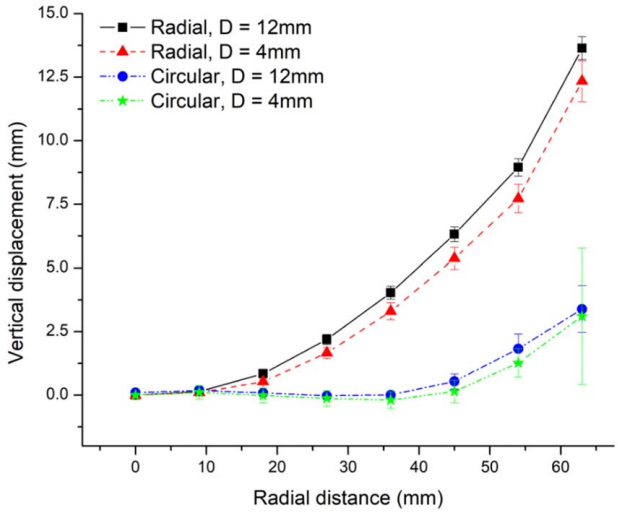

Fig. 16 Comparison between the average deflections of the bowl shape achieved using radial and circular scan paths. Standard deviations are shown. Much more deformation could be achieved using radial scan patterns.

From the results shown in Figs. 12–14, it can also be concluded that in the absence of in-plane strains, deformation can still be induced; however, the amount of deformation increases considerably if the bending strains in the top facesheet are mostly substituted by in-plane strains. To obtain curvatures of greater magnitude than those in Figs. 4 and 8, in-plane strains need to be induced across the entire sandwich panel thickness, which cannot be achieved using laser forming.

4.4 Effect of Scan Line Length. One issue that becomes important, due to the high thickness of metal foam sandwich panels, is the length of the laser scan path. To investigate the effect of the scan length, a circular scan pattern shown in Fig. 15 was compared with the radial scan pattern shown in Fig. 2(*a*). To allow for a meaningful comparison, a constant input energy was maintained. This was achieved by defining a circular scan pattern such that the overall scan length of the circular and radial scan patterns was identical for experiments of equal laser spot size. Several circular scan patterns with different spacings may satisfy this criterion, so no unique solution exists. Two scan patterns were investigated in this section. For the experimental results in Figs. 16 and 17, the pattern in Fig. 15 was used for the process condition of $D=$ 12 mm and $v=10$ mm/s, where the laser radii were (R_1, R_2, R_3, R_4) = (30, 36.5, 43.1, 49.6) millimeters. At $D=4$ mm and $v=$ 30 mm/s, the same overall area was scanned, but more laser scan lines were employed that were more closely spaced with the radii (R_1, R_2,…, R_{10}) = (30, 32.2, 34.4, 36.5, 38.7, 40.9, 43.1, 45.2, 47.4, 49.6) millimeters. For the numerical results in Figs. 18 and 19, on the other hand, a scenario was analyzed where the largest circular scan was only 10 mm away from the specimen edge. This scenario illustrated several points that could be used to explain the importance of the path length.

From Fig. 16, it can be seen that the circular scan pattern yielded significantly less bending than a radial scan pattern. Choosing a circular scan pattern with a larger spacing to the specimen edge increases the amount of bending, while a larger spacing decreases the amount of bending and can even cause delamination of the top facesheet.

In order to explain the difference between the deformation induced by the circular and radial scan patterns of equal energy input, the numerical results from Sec. 4.1 were compared with numerical results that were performed using a circular scan pattern (Fig. 17). The scan pattern used four concentric circles, where the outermost circle was very close to the specimen edge. No symmetry constraints were used in this simulation to capture the heat accumulation effects. The process condition was $D=$ 12 mm and $v=10$ mm/s, and the overall scan length was the same as in the radial pattern.

The temperature distributions were compared first, as shown in Fig. 18, during (a) a radial scan, (b) a circular scan far away from the specimen edge, and (c) a circular scan close to the specimen edge. For the circular scans, the temperature distributions are shown after three-fourth of a revolution. Comparing scenarios (a) and (b), it is apparent that while little heat reaches the bottom surface in a radial scan, much more heat reaches the bottom surface in circular scans due to pre-heating of the material. Moreover, the temperature gradients are farther apart, and there is a longer "trail" where the material underwent significant heating. All of these factors imply that the temperature gradient in circular scans is smaller and that the material surrounding the laser-irradiated material undergoes more heating. Hence, the thermal prerequisites of the bending mechanisms (TGM, UM, and MTGM) are not satisfied. The thermal prerequisites are even more poorly satisfied when the circular scan is performed very close to the edge (Fig. 18(*c*)). The reason is that the gradients become even smaller, and the material surrounding the irradiated region undergoes even more heating.

How well the thermal prerequisites of the bending mechanisms are met translates into how much plastic compressive strain is generated. This becomes clear from Fig. 17, where the maximum plastic strain magnitude is significantly lower than in the radial case in Fig. 6. Figure 19 confirms this finding, showing the plastic strain distribution at a cross section in the *yz*-plane at the center of circular specimen. Figure 19(*a*) shows an asymmetric plastic strain distribution, generated from performing the outermost laser scan. By the specimen edge (left side), little plastic compressive strain developed both in the top facesheet and in the foam core compared to the side that faces the center of the specimen (right side). The reason is that close to the edge, the surrounding material underwent more heating and thermal softening, and consequentially allowed for more thermal expansion of the laser-irradiated material. Thus, a lower amount of the thermal strains in the laser-irradiated material turned into plastic compressive strains. Figure 19(*b*) confirms that as the distance to the edge

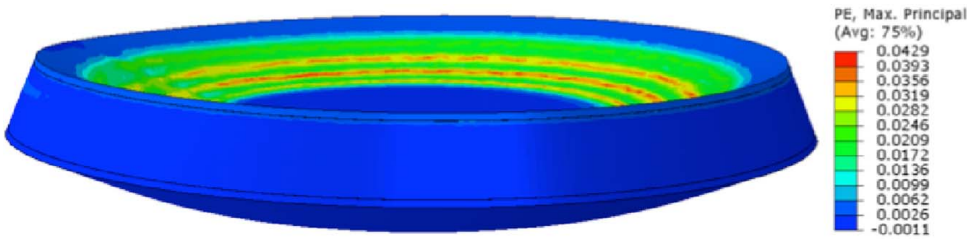

Fig. 17 Bowl shape obtained using a circular scan pattern. The spot size was $D=12$ mm and the scan speed was $v=10$ mm/s. The deformation was magnified by a factor of 10 for viewing clarity. The plastic strain magnitude is lower than when using a radial scan pattern (Fig. 6).

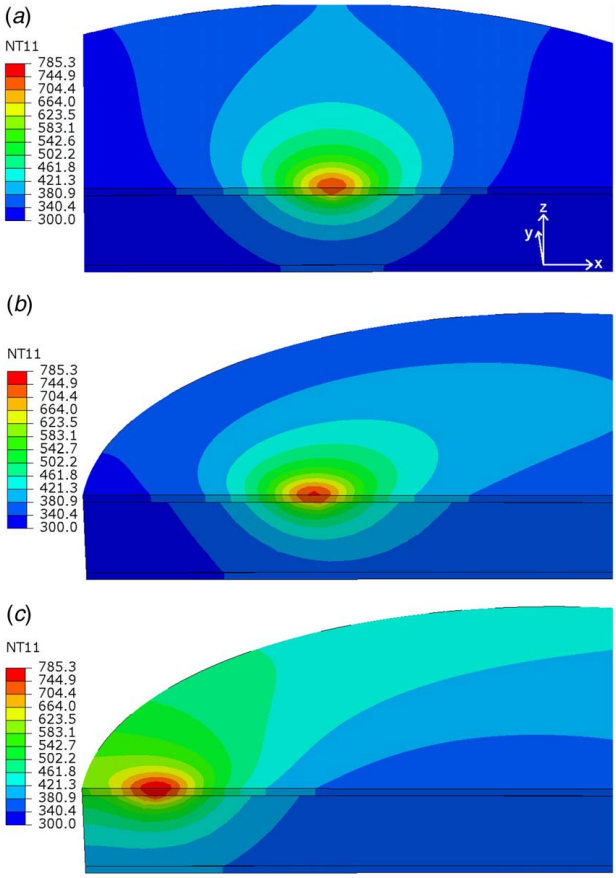

Fig. 18 Temperature distributions during (*a*) a radial laser scan, (*b*) a circular scan far away from the edge, and (*c*) a circular scan close to the edge. In circular scans, the temperature gradient is reduced, and the material surrounding the irradiated region undergoes more heating, especially if the scan is performed close to the edge.

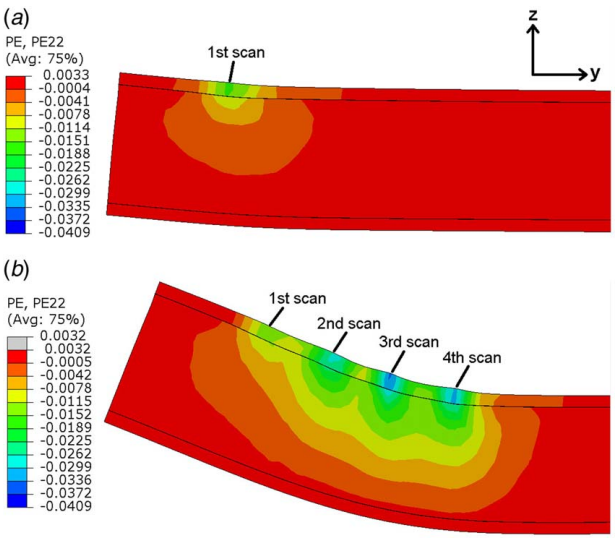

Fig. 19 Plastic strain distributions in *y*-direction after (*a*) a single laser scan close to the edge and (*b*) after four laser scans. The compressive strain increases with increasing distance from the edge, and its magnitude is higher on the side facing the center of the specimen.

increases (from the first to the fourth scans), the thermal prerequisite is better satisfied, and a higher amount of plastic compressive strain is generated.

In summary, it was shown that the scan path length becomes more important for metal foam sandwich panels, not because it changes the bending mechanisms, but because the thermal and mechanical prerequisites of the bending mechanisms are more difficult to satisfy. Especially for small specimens, the scan paths must be kept as short as possible.

5 Conclusions

This study demonstrated that laser forming could induce 3D deformation in metal foam sandwich panels. Both bowl and saddle shapes, the two fundamental non-Euclidean geometries, can be achieved under very different process conditions.

It was further shown that the mechanisms of laser-induced 3D bending are identical to laser forming of 2D geometries. At process conditions where the laser spot size is significantly smaller than the sheet thickness, only bending strains are present in the top facesheet and the foam core, and a moderate amount of deformation can be achieved. Increasing the laser spot size to the order of the sheet thickness converts most of the bending strains in the top facesheet to in-plane strains, and a slightly higher amount of deformation can be achieved. Even at large laser spot sizes, however, the 3D deformation is limited to moderate curvatures, because laser forming cannot induce in-plane strains throughout the entire sandwich panel section, which is necessary for producing large curvatures.

This study further showed that the choice of the scan path length is more important in metal foam sandwich panels than sheet metal, due to the larger thickness of the sandwich panels. The farther away laser scans are performed to the specimen edge, the better the thermal and mechanical prerequisites of the laser bending mechanisms are satisfied, yielding more bending deformation. Lastly, this study demonstrated that accurate 3D bending predictions can be achieved in numerical simulations using the same modeling techniques that applied to 2D laser forming.

Acknowledgment

The financial support from the National Science Foundation under a GOALI grant #CMMI-1725980 is gratefully acknowledged. This work used the Extreme Science and Engineering Discovery Environment (XSEDE) Stampede through allocation TG-DDM160002, which is supported by the National Science Foundation (Grant No. ACI-1548562) [25].

Nomenclature

v = laser scan speed
x = x-coordinate
y = y-coordinate
z = z-coordinate
A = absorption coefficient
D = laser beam diameter
F = yield surface parameter
H = hardening modulus
K = penalty stiffness
P = laser power
T = temperature
Y = yield strength
$\dot{Y}$ = rate of change of yield strength
h_σ = tangent modulus in uniaxial compression
h_p = tangent modulus in hydrostatic compression
t_n = normal traction
t_s = shear traction in first direction
t_t = shear traction in second direction

u_n = displacement in normal direction
u_s = displacement in first shear direction
u_t = displacement in second shear direction
K_{nn} = stiffness in normal direction
K_{ss} = stiffness in first shear direction
K_{tt} = stiffness in second shear direction
AE = area energy
α = aspect ratio of elliptical yield surface
ε = strain
$\dot{\varepsilon}_{ij}^{p}$ = plastic strain rate
ρ = density
σ = stress
σ_e = von Mises' equivalent stress
σ_m = mean stress
$\hat{\sigma}$ = equivalent stress

References

[1] Ashby, M. F., Evans, A. G., Fleck, N. A., Gibson, L. J., Hutchinson, J. W., and Wadley, H. N. G., 2000, *Metal Foams: A Design Guide*, Butterworth-Heineman, Washington, DC.
[2] Gibson, L. J., and Ashby, M. F., 1988, *Cellular Solids: Structure & Properties*, Pergamon, Oxford.
[3] Banhart, J., and Seeliger, H. W., 2012, "Recent Trends in Aluminum Foam Sandwich Technology," Adv. Eng. Mater., **14**(12), pp. 1082–1087.
[4] Banhart, J., and Seeliger, H. W., 2008, "Aluminium Foam Sandwich Panels: Manufacture, Metallurgy and Applications," Adv. Eng. Mater., **10**(9), p. 793.
[5] Bucher, T., Cardenas, S., Verma, R., Li, W., and Yao, Y. L., 2018, "Laser Forming of Sandwich Panels With Metal Foam Cores," ASME J. Manuf. Sci. Eng., **140**(11), p. 111015.
[6] Bucher, T., Zhang, M., Chen, J. J., Verma, R., Li, W., and Yao, Y. L., 2019, "Laser Forming of Metal Foam Sandwich Panels: Effect of Manufacturing Method," ASME J. Manuf. Sci. Eng., **141**(5), p. 051006.
[7] Banhart, J., 2003, "Aluminum Foams: On the Road to Real Applications," MRS Bull., **28**(4), pp. 290–295.
[8] Kennedy, A., 2012, *Powder Metallurgy, Porous Metals and Metal Foams Made From Powders*, InTech, Rijeka, Croatia, Chap. 2.
[9] Mata, H., Santos, A., Parente, M., Valente, R., Fernandes, A., and Jorge, N., 2013, "Study on the Forming of Sandwich Shells With Closed-Cell Foam Cores," Int. J. Mater. Form., **7**(4), pp. 413–424.
[10] Contorno, D., Filice, L., Fratini, L., and Micari, F., 2006, "Forming of Aluminum Foam Sandwich Panels: Numerical Simulations and Experimental Tests," J. Mater. Process. Technol., **177**(1–3), pp. 364–367.
[11] Tavakoli, A., Naeini, H. M., Roohi, A. H., Gollo, M. H., and Shahabad, S. I., 2017, "Determining Optimized Radial Scan Path in 3D Laser Forming of SteelAISI 304 Plates to Produce Bowl Shapes," Int. J. Adv. Manuf. Technol., **91**(9–12), pp. 3457–3465.
[12] Tavakoli, A., Naeini, H. M., Roohi, A. H., Gollo, M. H., and Shahabad, S. I., 2017, "Optimization of Circular Scan Path to Produce Bowl Shapes in 3D Laser Forming Process," J. Laser Ap., **29**(4), p. 042001.
[13] Edwardson, S. P., Watkins, K. G., Dearden, G., and Magee, J., 2001, "3D Laser Forming of Saddle Shapes," Proceedings of the LANE '01, Erlangen, Germany, Aug. 28–31, pp. 559–568.
[14] Edwardson, S. P., Moore, A. J., Abed, E., McBride, R., French, P., Hand, D. P., Dearden, G., Jones, J. D. C., and Watkins, K. G., 2004, "Iterative 3D Laser Forming of Continuous Surfaces," Proceedings of the ICALEO '04, San Francisco, CA, Oct. 4–7, pp. 1–10.
[15] Cheng, J., and Yao, Y. L., "Process Design of Laser Forming for Three Dimensional Thin Plates," ASME J. Manuf. Sci. Eng., **126**(2), pp. 217–225.
[16] Liu, C., and Yao, Y. L., 2005, "FEM-Based Process Design for Laser Forming of Doubly Curved Shapes," J. Manuf. Proc., **7**(2), pp. 109–121.
[17] Bucher, T., Young, A., Zhang, M., Chen, C. J., and Yao, Y. L., 2018, "Thermally Induced Mechanical Response of Metal Foam During Laser Forming," ASME J. Manuf. Sci. Eng., **140**(4), p. 041004.
[18] Vollertsen, F., 1993, "The Mechanisms of Laser Forming," CIRP Ann., **42**(1), pp. 301–304.
[19] Hanssen, A. G., Girard, Y., Olovsson, L., Berstad, L., and Langseth, M., 2006, "A Numerical Model for Bird Strike of Aluminium Foam-Based Sandwich Panels," Int. J. Impact Eng., **32**(7), pp. 1127–1144.
[20] Spittel, T., Spittel, M., and Warlimont, H., 2011, *Non-Ferrous Alloys—Light Metals Vol.VIII/2C2, AlSi8*, Springer, Berlin, Germany.
[21] Deshpande, V., and Fleck, N., 2000, "Isotropic Constitutive Models for Metallic Foams," J. Mech. Phys. Solids, **48**(6–7), pp. 1253–1283.
[22] Bucher, T., Bolger, C., Zhang, M., Chen, C., and Yao, Y. L., 2016, "Effect of Geometrical Modeling on Prediction of Laser-Induced Heat Transfer in Metal Foam," ASME J. Manuf. Sci. Eng., **138**(12), p. 121008.
[23] Turon, A., Davila, C. G., Camanho, P. P., and Costa, J., 2007, "An Engineering Solution for Mesh Size Effects in the Simulation of Delamination Using Cohesive Zone Models," Eng. Fract. Mech., **74**(10), pp. 1665–1682.
[24] Skidmore, M., and Johnson, R., 1989, "Thermal Contact Conductance of Various Metals at Elevated Temperatures," Proceedings of 24th Thermophysical Conference, Raleigh, NC, June 12–14, pp. 1–8.
[25] Towns, J., Cockerill, T., Dahan, M., Foster, I., Gaither, K., Grimshaw, A., Hazlewood, V., Lathrop, S., Lifka, D., Peterson, G. D., Roskies, R., Scott, J. R., and Wilkins-Diehr, N., 2014, "XSEDE: Accelerating Scientific Discovery," Comput. Sci. Eng., **16**(5), pp. 62–74.